Density Functional Theory Study of the Oxygen Chemistry and NO Oxidation Mechanism on Low-Index Surfaces of SmMn₂O₅ Mullite

Zhengzheng Chen,[†,⊥] Xiao Liu,[‡,⊥] Kyeongjae Cho,[§] Rong Chen,*[‡] and Bin Shan*[†,§]

[†]State Key Laboratory of Materials Processing and Die and Mold Technology and School of Materials Science and Engineering, [‡]State Key Laboratory of Digital Manufacturing Equipment and Technology and School of Mechanical Science and Engineering, Huazhong University of Science and Technology, Wuhan 430074, Hubei People's Republic of China

[§]Department of Materials Science and Engineering, The University of Texas at Dallas, Richardson, Texas 75080, United States

S *Supporting Information*

ABSTRACT: SmMn₂O₅ mullite has recently been reported to be a promising alternative to traditional Pt-based catalysts for environmental and energy applications. By performing density functional theory calculations, we have systematically investigated lattice oxygen reactivity and oxygen adsorption/dissociation/migration behaviors on low-index surfaces of SmMn₂O₅ mullite with different terminations. On the basis of the oxygen chemistry and thermodynamic stability of different facets, we conclude that $(100)^{3+}$, $(010)^{4+}$, and $(001)^{4+}$ are reactive toward NO oxidation via either the Mars van Krevelen (MvK) or Eley−Rideal (ER) mechanism. Concrete $NO \rightarrow NO_2$ reaction paths on these candidate mechanisms have also been calculated. Both the $(010)^{4+}$ and $(001)^{4+}$ surfaces presented desirable activities. Bridge MnO sites on $(010)^{4+}$ surface are identified to be the most active for NO oxidation through the ER mechanism with the lowest barrier of ∼0.38 eV. We have also identified that on all active sites considered in the current study, the rate-determining step in $NO \rightarrow NO_2$ oxidation reaction is the NO_2 desorption. Our study gives an insight into the mechanisms of NO oxidation on SmMn₂O₅ mullite at the atomic level and can be used to guide further improvement of its catalytic performance.

KEYWORDS: oxygen chemistry, NO oxidation, SmMn₂O₅ mullite, density functional theory calculations
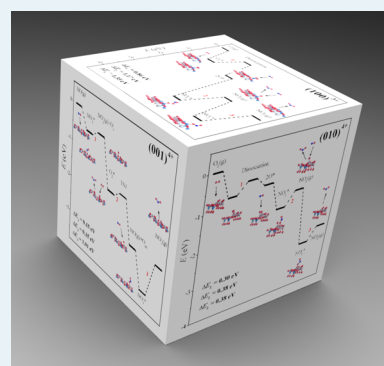
1. INTRODUCTION

Transition metal oxides (TMOs) have recently attracted great attention as promising catalysts for many important environmental and clean energy applications (e.g., hazardous exhausts cleaning, solid oxide fuel cells).[1−4] TMOs are popular because of their facile economical and scalable synthesis, high catalytic activities of redox reactions, and good durability and thus are expected to be viable alternatives to precious metal catalysts. Previous studies have accomplished much progress in finding highly efficient TMOs catalysts. Co₃O₄ and RuO₂ are reported as excellent catalysts for CO oxidation.[5−8] Misono et al. have reported that Mn₂O₃ reveals low-temperature NO oxidation performance and can enhance the NOₓ removal during the selective catalytic reduction (SCR) by hydrocarbons.[9] Ceria-modified MnOₓ also shows high activity for the SCR of NOₓ with ammonia and excellent sulfur resistance.[10]

However, redox reactions can add or remove oxygen (depending on an oxidizing or reducing reaction environment) from simple TMO, leading to an oxide phase change with different stoichiometry. Such a stoichiometry change will inevitably modify the metal oxidation state, leading to reduced catalytic activity or deactivation. For this reason, simple TMOs are known to experience surface phase change and the corresponding loss of catalytic activity during an extended period of catalytic reactions.[11] In recent decades, complex metal oxides with ABₘOₙ structure have received great attention in

catalytic applications as a result of more stable atomic structures under reacting environments based on the backbone structure of connected metal−oxygen polyhedra. Kim et al. have shown that La-based perovskite oxide (ABO₃) can be used as effective automotive emission control catalysts with performance rivaling that of commercial platinum.[12] Perovskite phase TMOs have also been used as mixed ionic and electronic conductors for high temperature applications.[13−17] More recently, K. Cho et al. found a family of complex oxides, mullites (with SmMn₂O₅ as a prototypical representative) to exhibit excellent catalytic activities for NO oxidation as a diesel engine oxidation catalyst.[18] This is a noteworthy finding because mullite-based oxides are significantly less expensive and more abundant than platinum group metals and offer a promising alternative route for tackling the oxygen activation problems. Moreover, the coexistence of both Mn³⁺ and Mn⁴⁺ metal ions in the mullite bulk structure as well as the formation of Mn−Mn surface dimers along the c-axis lead to rich and interesting local surface structures that greatly expand the tunability of the electronic structure of the active sites for NO oxidation.

On the theoretical side, the catalytic reaction processes on TMO surfaces are generally more complicated than that on a
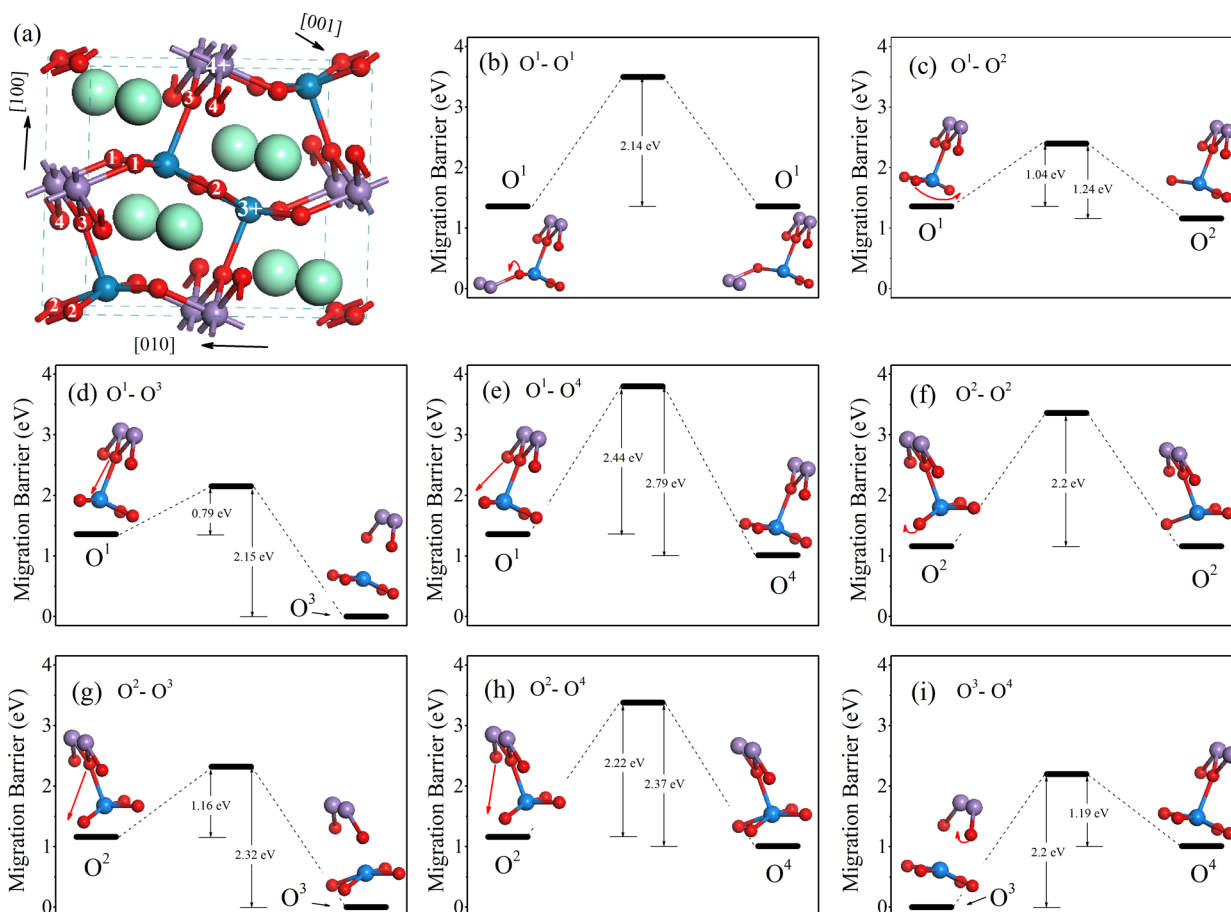
Figure 1. (a) Atomic structure of SmMn$_2$O$_5$. Green, red, violet, and blue spheres represent Sm, O, Mn^{4+}, and Mn^{3+} ions, respectively. Nonequivalent O positions are labeled as 1−4 superscripts. (b−i) MEPs of eight migrating paths between different V$_O$'s. The red arrows represent the migrating direction of the involved O atom.

clean metal surface, as both the adsorbed oxygen and lattice oxygen species could contribute to reactivity. In a typical oxidation reaction, TMOs can either serve as substrates where adsorbed reactants react with each other (Langmuir−Hinshelwood mechanism, LH, or Eley−Rideal mechanism, ER) to form new molecules[19−21] or contribute the lattice oxygen species to the oxidation process and subsequently be restored to the original state via oxygen dissociation and vacancy migrations (Mars−van Krevelen mechanism, MvK).[22] In some cases, multiple reaction routes, all contributing considerably to the total conversion rate, have been observed.[23,24] The oxygen chemistries and NO oxidation mechanisms on selected perovskites, such as LaCoO$_3$ and LaMnO$_3$, have been reported.[25−29]

In contrast, the high activities of SmMn$_2$O$_5$ for NO oxidation have not been well understood yet. It has been proposed that Mn dimers on stepped (110) surfaces are active sites toward NO oxidation via the ER mechanism based on density functional theory (DFT) calculations.[18] Although the aforementioned calculations have presented a persuasive perspective on catalytic activities of SmMn$_2$O$_5$ for NO oxidation, the modeling analysis in the previous work[18] is limited only to (110) surface termination exposing the Mn^{4+} atomic chains (forming dimers) and the MvK reaction mechanism of NO adsorption, NO$_2$ desorption, and subsequent O$_2$ adsorption. Under high oxygen pressure conditions in typical diesel engines,[30] it is likely that other surface active sites will also

contribute to the overall activity. A systematic and comprehensive study of SmMn$_2$O$_5$ surfaces taking into account both surface stability and catalytic activity is still lacking, to the best of our knowledge. Because the catalytic performance of metal oxides is greatly influenced by surface orientations, oxygen-vacancy configurations, and valence states of transition metal ions, it is of great importance to gain deeper insight into these factors and to clarify the oxygen chemistries in SmMn$_2$O$_5$ mullites. Such understanding serves as the necessary step toward further improving and optimizing mullites' performance for energy and environmental applications.

In this work, we have performed DFT calculations to study the oxygen chemistry in bulk SmMn$_2$O$_5$ phases as well as four low index surfaces—(110), (100), (010) and (001)—with different surface terminations. Our results show that both ER and MvK mechanisms coexist in NO oxidation by SmMn$_2$O$_5$. The most active surface is the (010) facet, with Mn^{4+} ions in the surface layer where oxidation can be realized by a synergetic mechanism involving ER processes along bridge-MnO channels. The (001) surface with Mn^{4+} ions in the surface layer is also expected to be active for oxidation via the MvK mechanism. On the other hand, despite the low oxygen vacancy formation energy, the (110) surface could easily undergo surface reconstruction and quickly lose active sites. Our calculations also suggest that the rate-determining step of oxidation reaction on SmMn$_2$O$_5$ surfaces is the desorption of NO$_2$ on both (010) and (001) facets.

Table 1. E_{V_O} (eV) on Different O Sites in SmMn$_2$O$_5$ Bulk and on Low-Index Surfaces^a

	O^1	O^2	O^3	O^4
bulk	4.21 (1.10e)	4.01 (1.11e)	2.85 (0.95e)	3.86 (1.13e)
(110)$^{4+}$	0.96 (0.77e)		2.98 (0.84e)	2.83 (0.96e)
(110)$^{3+}$		3.39 (O^2(I)) (1.01e)		
		4.38 (O^2(II)) (1.18e)		
(100)$^{4+}$	2.73 (0.97e)	1.53 (0.89e)		4.37 (1.17e)
(100)$^{3+}$	4.75 (0.96e)	4.92 (1.18e)	4.37 (0.90e)	3.46 (1.00e)
(010)$^{4+}$		1.14 (0.77e)	2.15 (0.80e)	2.81 (0.89e)
(010)$^{3+}$	2.17 (0.91e)		3.28 (1.02e)	3.75(1.07e)
(001)$^{4+}$	2.01 (0.82e)	0.87 (0.77e)		
(001)$^{3+}$			3.79 (0.88e)	

^{a}The numbers in parentheses in the "bulk" row are the electrons accumulation of the O atom at different sites based on Bader analysis, where "e" means unit charge.

The rest of the paper is organized as follows: the computational methods are presented in Section 2. Detailed results and discussions on migration of oxygen vacancies, evolution of adsorbed O$_2$ molecules, and NO oxidation routes are shown in Section 3. Finally, we present a conclusion in Section 4.

2. COMPUTATIONAL METHODS

All DFT[31,32] calculations in this work were performed with the Vienna Ab Initio Simulation Package (VASP).[33−35] Generalized gradient approximation (GGA) with Perdew−Burke−Ernzerhof (PBE)[36] form was employed to describe the exchange and correlation energy. Electron−ion interactions were treated within the projector augmented wave (PAW)[37] method. An energy cutoff of 400 eV is employed on the plane wave basis. We used a Monkhorst−Pack[38] k-mesh of 7 × 7 × 7 for the bulk, 5 × 5 × 1 for the (001) surface, 7 × 5 × 1 for (010), 5 × 7 × 1 for (100) surfaces, and 7 × 3 × 1 for the (110) surface, respectively. More details about the size and calculation settings of the slab can be found in the Supporting Information (SI). The Fermi broadening scheme with a smearing width of 0.05 eV is used for numerical integration in the first Brillouin zone. To check the convergence, we have compared the total energy with the ones calculated with a finer k-mesh. The difference is smaller than 5 meV. The SmMn$_2$O$_5$ surfaces were represented by periodic slabs with a thickness of at least 10 Å. A vacuum with thickness of 15 Å is adopted to avoid interaction between the image slabs. In both bulk and surface calculations, the geometry optimization is performed until the Hellmann−Feynman force on each unconstrained atom is smaller than 0.03 eV/Å. Because Mn ions in SmMn$_2$O$_5$ possess magnetic moments, the total energy calculations are carried out with spin polarization. We note that standard DFT methods may have limitations in describing the electronic structure for transition metal oxides and rare-earth compounds with strong correlation, which can be improved by using higher-level methods, such as GW[39,40] or hybrid functionals.[41,42] However, considering the large surface unit cells that are required in modeling catalytic reactions and the related high computational cost, standard DFT calculation is adopted, which has also been shown to be of reasonable accuracy in describing reaction energies of similar systems.[18,25]

To discuss the thermodynamic stability of surfaces, we have calculated the surface grand potential (Ω), which has been previously used in studies of low-index surfaces of binary and ternary compounds.[43,44] The detailed computational process can be found in the SI. For the minimum energy path (MEP)

of important elementary steps (including the diffusion of O vacancies (V_O) and atomic O, the dissociation of molecular O$_2$ and the NO oxidation processes), the climbing-image nudged elastic band (CI-NEB)[45] method was employed. Initial images along reaction paths are obtained by linear interpolation between the reactant and product configurations. Six intermediate images were used for all CI-NEB calculations, which map the MEP with reasonable accuracy.

3. RESULTS AND DISCUSSION

3.1. Diffusion of Oxygen Vacancies in SmMn$_2$O$_5$ Bulk.

The crystal structure of SmMn$_2$O$_5$ is shown in Figure 1a, which has *Pbam* space group symmetry. The calculated lattice constants and magnetic moment (μ) are a = 7.43 Å, b = 8.59 Å, c = 5.70 Å, and μ = 6.36 μ_B, which are in good agreement with previous experimental studies.[46,47] As shown in Figure 1a, O and Mn ions form a network of polyhedra as the backbone with Sm ions accommodated within the pores enclosed by polyhedra. It should be noted that Mn ions in SmMn$_2$O$_5$ sit in two types of local environments, 50% of which are at centers of stretched MnO$_6$ octahedra labeled as Mn^{4+}; the other 50% of the Mn ions are in MnO$_5$ pyramids labeled as Mn^{3+}. There exist four nonequivalent positions of O ions in the SmMn$_2$O$_5$ bulk as a result of its symmetry: O^1, O^2, and O^4 sites are connected to two Mn ions, and an O^3 site is connected to three Mn ions. The calculated oxygen vacancy formation energy, E_{V_O} at each site is listed in Table 1. The E_{V_O} is defined as

$$E_{V_O} = E_{\text{sys-O}} - E_{\text{sys}} + E_{O_2}/2 \tag{1}$$

where E_{sys} and $E_{\text{sys-O}}$ are the total energies of ideal and defective (with an O vacancy) SmMn$_2$O$_5$ (bulk or slabs), respectively, and E_{O_2} is the energy of an O$_2$ molecule. The lowest E_{V_O} in the bulk appears at the O^3 site (2.85 eV), where the O atom is connected to a Mn^{3+} ion and two Mn^{4+} ions. The formation energy of vacancy at O^3 sites is much lower than those at other oxygen sites, indicating the preference of oxygen vacancies at O^3 sites. Compared with the oxygen vacancy formation energy in SmMnO$_3$ perovskite,[48] E_{V_O} at the O^3 site in mullite is lower, indicating a potential use of SmMn$_2$O$_5$ as cathode materials for solid oxide fuel cells.

We have further enumerated all the different diffusion paths of V_O in the bulk, shown in Figure 1b−i. Generally speaking, the migration barrier energy of $E_m(V_O)$ in bulk SmMn$_2$O$_5$ ranges from 0.97 to 2.81 eV. These relatively high barriers are due in part to the low E_{V_O} at the O^3 site, which leads to the

stability of the vacancy at the O^3 site compared with other defect sites. One should also note that there are several competing migration paths for V_O diffusion because of similar heights of migration barriers: After a V_O is formed at the O^3 site, it can move either along the $[\bar{1}10]$ direction to an O^1 site (Figure 1d) or along the $[001]$ direction to an O^4 site (Figure 1i). However, once the oxygen vacancy diffuses to an O^1 site adjacent to O^3, there is no continuous $O^3 \rightarrow O^1 \rightarrow O^3$ channel along the $[\bar{1}10]$ direction for further diffusion. The vacancy has to migrate from the O^1 site either to a neighboring O^1 site or to an O^2 site, as illustrated in Figure 1a. Once it overcomes the relatively high barrier of 2.11 eV for hopping to O^1 sites, it can then be connected to another O^3 site and continue the bulk diffusion. Along the $[001]$ direction, the oxygen vacancy bulk diffusion has to overcome the migration barrier between $O^2 \rightarrow O^2$ sites and $O^2 \rightarrow O^4$ sites to form a continuous path. Clearly, in all the paths that we have considered, the O^3 sites serve as traps for V_O diffusion because all the barriers connecting two O^3 sites are higher than 2.0 eV. The results of the V_O diffusion barrier can also be used to qualitatively discuss the segregation tendency of V_O to different surfaces, which might affect the activities for NO oxidation. The discussions are presented in the following sections.

To gain insight into the exceptionally low E_{V_O} at the O^3 site compared with other oxygen sites, we have carried out the Bader charge analysis,[49] which gives a reliable estimation of the electron accumulation on O atoms at different sites (Table 1). Note that the reference state is taken as an isolated O atom with six valence electrons. Although the O atom at the O^3 site forms more bonds to neighboring Mn ions, the gained electrons of the O atom at the O^3 site are $\sim$0.15−0.20e less than that on the other sites, which indicates that the O atom at the O^3 site forms weaker ionic bonds to neighboring Mn ions. In addition, we have compared the structural relaxations caused by the formation of V_O at the O^3 or O^4 site, respectively. The change in distances between Mn atoms nearest to the V_O (Δd_{Mn-Mn}) and average of displacements of all atoms in $SmMn_2O_5$ bulk (s_{rms}) were chosen to represent the structural relaxation. The results are listed in Table 2. Note that there are

Table 2. Structural Relaxation Due to the Nucleation of a Vacancy at O^3 or O^4 Site[a]

	O^3			O^4
d_{Mn-Mn} (Å)	0.13	0.13	0.20	0.27
d_{Mn-Mn}/d^0	3.8%	3.8%	7.7%	8.8%
s_{rms} (Å)	0.027			0.042

[a]In the third row, d^0 is the distance between Mn atoms in the ideal $SmMn_2O_5$ bulk.

three values of Δd_{Mn-Mn} for the O^3 site because the O^3 site connects to three Mn atoms. Both Δd_{Mn-Mn} and s_{rms} are smaller, with the V_O at the O^3 site. Therefore, when a V_O is nucleated at the O^3 site, the local atomic structure is less affected, which can also be attributed to the weaker interactions with neighbor atoms, as suggested by the Bader charge analysis. Therefore, it is easier to remove the O atoms at the O^3 sites from the bulk, forming a stable oxygen vacancy compared with other O sites.

3.2. Oxygen Chemistry on $SmMn_2O_5$ Surfaces. Understanding the surface oxygen chemistry of $SmMn_2O_5$ is critical in elucidating the origin of catalytic activity for NO oxidation. According to the symmetry of $SmMn_2O_5$, there are multiple

nonequivalent low index surfaces and terminations. We have considered four families of low-index surfaces in the present work: {110}, {100}, {010}, and {001}, some of which have been observed in previous experimental studies.[18,50] For each family, we have built up two terminations: one contains Mn^{3+} ions (labeled as $(hkl)^{3+}$) and another contains Mn^{4+} ions (labeled as $(hkl)^{4+}$), respectively. In the following subsections, we will discuss oxygen chemistry, such as formation of surface oxygen vacancies, dissociation of adsorbed oxygen molecule, and migration of surface oxygen atoms. Before the detailed discussions, it is necessary to define adsorption energy of an O_2 molecule ($E_{ad}(O_2)$) and an O atom ($E_{ad}(O)$) on surfaces:

$$E_{ad}(O_2) = E_{slab+O_2} - E_{slab} - E_{O_2} \tag{2}$$

$$E_{ad}(O) = E_{slab+O} - E_{slab} - E_{O_2}/2 \tag{3}$$

In eqs 2 and 3, E_{slab}, E_{slab+O_2}, and E_{slab+O} are the total energies of ideal $SmMn_2O_5$ slabs, a slab with single adsorbed O_2 molecule, and a slab with single adsorbed O atom, respectively. E_{O_2} is the energy of an O_2 molecule, the same as in eq 1.

(110) Surfaces. Figure 2a,d presents the relaxed structures of $(110)^{4+}$ and $(110)^{3+}$, respectively. The O^3 and O^4 ions on the $(110)^{4+}$ surface show slight buckling. There are two kinds of Mn−O channels on the $(110)^{4+}$ surface: one is labeled as bridge-MnO, along which O^3 and O^4 lie at the bridge of two Mn^{4+} ions and binds to both of them, and the other is labeled as atop-MnO, which is made of Mn^{4+} and O^1, where an O^1 site is at the top of a Mn^{4+} ion. In Table 1, we have listed the results of E_{V_O} at different sites. On the $(110)^{4+}$ surface, the $E_{V_O}(O^1)$ is exceptionally low at 0.96 eV, and $E_{V_O}(O^3)$ is 2.98 eV, which is comparable to that in bulk. The low $E_{V_O}(O^1)$ suggests that O atoms at O^1 sites can be easily removed from the $(110)^{4+}$ surface and participate in the NO oxidation reaction. Thus, the NO oxidation can proceed through the MvK mechanism, which is consistent with the experimental observation that the surface O species is consumed during the NO oxidation in O-poor condition.[18] In addition, since $E_{V_O}(O^1)$ on the $(110)^{4+}$ surface is much lower than that in the bulk, the segregation tendency of vacancies in bulk to the $(110)^{4+}$ surface is expected to be strong. However, since the migration barrier from an O^3 site is around 2.2 eV, the segregation could not be efficient at low temperature.

Interestingly, we found that the creation of a vacancy at an O^1 site causes local reconstruction: one neighboring O^1 atom spontaneously moves to the bridge position between two Mn^{4+} ions, as shown in Figure 2b. Therefore, strictly speaking, once a V_O at an O^1 site forms, it self-destructs and is transformed into a bridge-O^1 configuration, referred as O^1_{Bn}. Because $E_{V_O}(O^1)$ is less than 1 eV, it is worthwhile to estimate the concentration of O^1 atoms at room temperature. Following previous studies,[25,51] we have simulated the nucleation of vacancies at O^1 sites by using the first-order desorption kinetics model. The details are included in the SI. Figure S3 shows that the concentration of the vacancies at O^1 sites reaches 4.6% at 300 K. This result suggests that at room temperature, reconstruction of the $(110)^{4+}$ surface is observable. Figure 2b also depicts that the O^1_{Bn} is considerably mobile along the $Mn^{4+}-O^1$ channel because the migration barrier, $E_m(O^1_{Bn})$, is 0.76 eV. On the other hand, O^1_{Bn} is very stable because it requires 4.22 eV to detach from the surface. Consequently, this atop-MnO O^1-to-O^1_{Bn} reconstruction will lead to loss of catalytic activities for NO
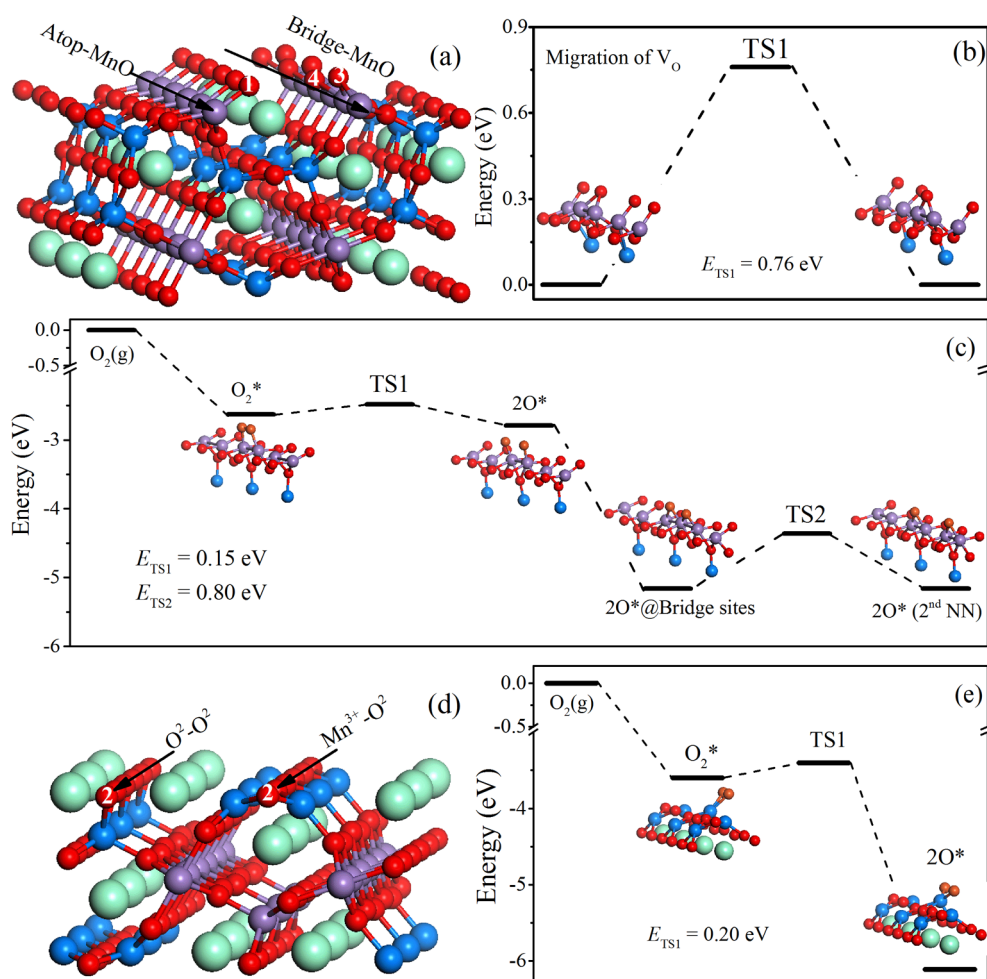
Figure 2. (a) Atomic structure of the $(110)^{4+}$ surface. (b) MEP of V_O migration along the channel of atop-MnO. (c) MEPs of adsorption/dissociation of an O_2 molecule on the $(110)^{4+}$ surface. (d) Atomic structure of the $(110)^{3+}$ surface. (e) MEPs of adsorption/dissociation of an O_2 molecule on the $(110)^{3+}$ surface.

oxidation when the MvK mechanism is prevailing. This may be related to the aging mechanism of the $SmMn_2O_5$ during the NO oxidation operation, which will be discussed in detail in Section 3.3.

We have also obtained an energetic scenario of the dissociation of a gaseous O_2 molecule to two isolated O adatoms on the $(110)^{4+}$ surface in Figure 2c. An O_2 molecule can adsorb onto Mn^{4+} ions in both channels: the adsorption energy $(E_{ad}(O_2))$ is -2.63 eV and -1.95 eV in atop-MnO and bridge-MnO channels, respectively. We have focused on the atop-MnO channel because it has stronger binding to O_2 molecules. The dissociation of an adsorbed O_2 molecule into the two nearest O adatoms is facile and requires only a relatively low dissociation barrier (E_{dis}) of 0.15 eV. The dissociation is an exothermic process, lowering the system energy by 0.16 eV. The adsorption energy of an O atom, $(E_{ad}(O))$ is -1.39 eV. The dissociated O atoms that sit atop Mn ions will further relax to the bridge sites with further lowering of the total energy by 2.26 eV. Thus, $E_{ad}(O)$ in the most stable configuration is -2.58 eV, suggesting a strong binding interaction. Consequently, the adsorbed O species may not be active for NO oxidation via the ER mechanism. On the other hand, the barrier of an O adatom for migrating along the atop-MnO channel is 0.80 eV, indicating the mobility of O adatoms on the $(110)^{4+}$ surface is comparable to that of O_{Bn}^1.

Their interaction is thus worth investigating, as discussed in Section 3.3.

The $(110)^{3+}$ surface, on the other hand, presents a quite different energetic scenario. One channel of $Mn^{3+}-O^2$ can be identified on the $(110)^{3+}$ surface. One should note that there are also O^2-O^2 channels in the [001] direction bonding to Mn^{3+} ions in the sublayer. As listed in Table 1, the E_{V_O} in the $Mn^{3+}-O^2$ channel $(O^2(I))$ is as high as 3.39 eV. To create a V_O at an O^2 site in O^2-O^2 channels $(O^2(II))$ requires an even higher energy of 4.38 eV. Because the oxygen vacancy concentration is expected to be very low as a result of the large vacancy formation energy, the mobility of the V_O on this surface is ignored. On the other hand, the bare Mn^{3+} ions bond strongly to the O_2 molecules. As shown in Figure 2e, $E_{ad}(O_2)$ is -3.60 eV. After overcoming a low barrier of 0.20 eV, the adsorbed O_2 molecule dissociates to two adsorbed O atoms with a binding energy of -3.06 eV per atom. Note that the Mn^{3+} ion presents an apparent out-of-plane displacement during the dissociation. Because of the strong binding, it is difficult for the adsorbed O atoms to detach from the Mn^{3+} ions, and thus, they are unlikely to contribute to NO oxidation activity. In addition, because of the long distance between the Mn^{3+} ions (7.9 Å), the adsorbed O atoms cannot migrate along the $Mn^{3+}-O^2$ channel. On the basis of these considerations, the $(110)^{3+}$ surface is unlikely to present potential activities for NO
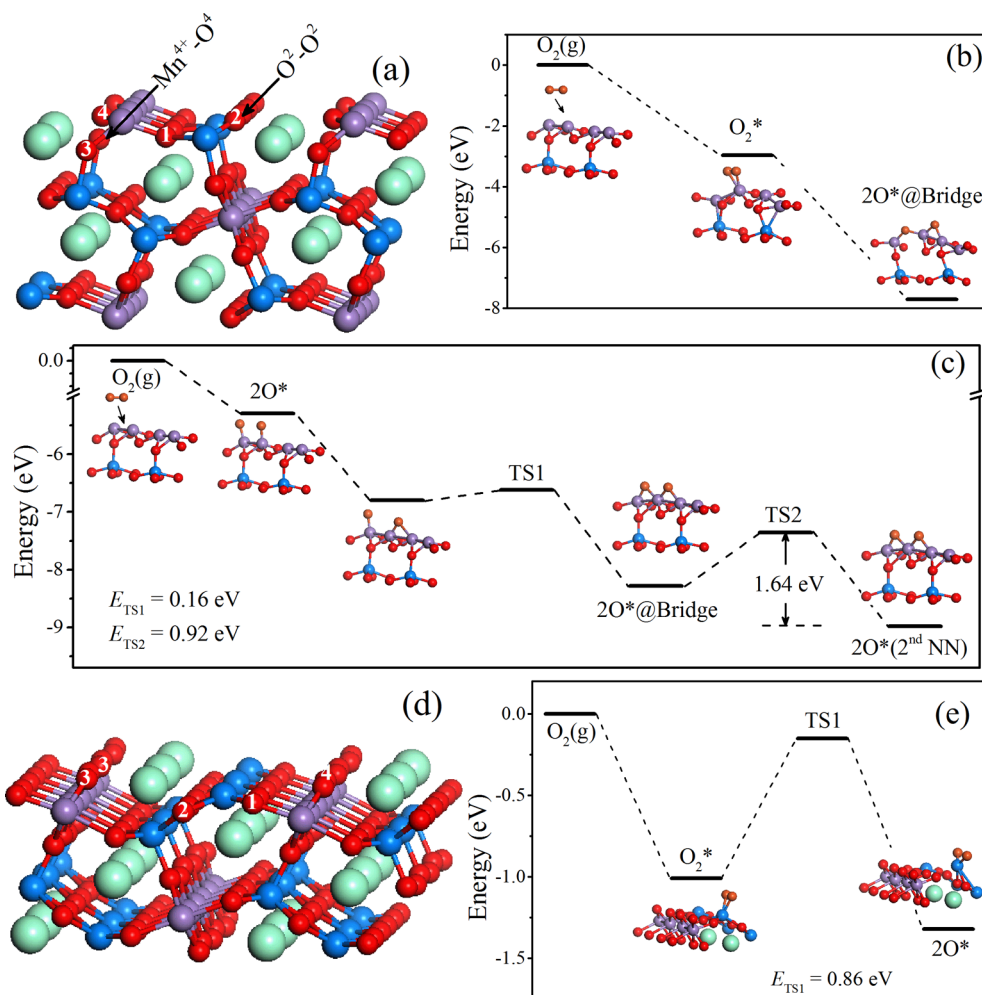
Figure 3. (a) Atomic structure of the $(100)^{4+}$ surface. (b) MEP of adsorption and dissociation of an O_2 molecule (monodentate) on the $(100)^{4+}$ surface. (c) MEP of adsorption and migration of an O_2 molecule (bidentate) on the $(100)^{4+}$ surface. (d) Atomic structure of the $(100)^{3+}$ surface. (e) MEP of adsorption and dissociation of an O_2 molecule on the $(100)^{3+}$ surface.

oxidation and can be easily passivated in an O-rich environment.

(100) Surfaces. Figure 3a,d presents the relaxed structures of $(100)^{4+}$ and $(100)^{3+}$ surfaces, respectively. The $(100)^{4+}$ surfaces is the only surface showing substantial reconstruction. Figure 3a shows that O atoms at the O^4 sites beneath the Mn^{4+} ion move upward and wrap up Mn^{4+} ions to prevent them from being exposed to a vacuum. Different O sites on the $(100)^{4+}$ surface present distinct vacancy formation energies. The lowest E_{V_O} is found at the O^2 site as 1.53 eV, whereas $E_{V_O}(O^4)$ is as high as 4.37 eV. Because the $E_{V_O}(O^2)$ on the $(100)^{4+}$ surface is lower than $E_{V_O}(O^3)$ in bulk, a V_O at an O^3 site in a sublayer is energetically favorable to diffuse to the $(100)^{4+}$ surface. However, the diffusion of V_O along the path O^3–O^2 might not be very efficient because of the diffusion barrier of 2.3 eV. A pair of O atoms at O^2 sites bond to a Mn^{3+} ion beneath the surface. The formation of a vacancy at an O^2 site makes its nearest O atom move to the atop position of the Mn^{3+} ion (see Figure S1 in the SI) and causes a stronger binding between this O atom and the Mn^{3+} ion (E_{V_O} = 1.74 eV).

Along the Mn^{4+}-O^4 channel, there are two adsorption configurations for an O_2 molecule: monodentate (Figure 3b) and bidentate (Figure 3c). By performing systematic

calculations, we have identified that a monodentate O_2 molecule adsorbs to one Mn^{4+} ion with $E_{ad}(O_2)$ = −2.97 eV (Figure 3b), with a subsequent dissociation into two O atoms located at adjacent bridge sites. Along the dissociation path of an O_2 molecule, no barrier is observed. The O_2 dissociation without a barrier on the Mn^{4+} dimer has also been reported in previous work.[18] The surface structure undergoes serious displacements, with one O adatom incorporated into the middle of a Mn^{4+} pair. A bidentate O_2 molecule, on the other hand, will automatically dissociate to two O atoms, each of which is at the atop position of a Mn^{4+} ion, as shown in Figure 3c. The average $E_{ad}(O)$ is −2.65 eV. In the subsequent relaxation process, one O atom slides to a bridge site between two Mn^{4+} ions, and the other atom overcomes a barrier of 0.16 eV and migrates to the nearest bridge site.

The last step in Figure 3c shows that the system energy could be further lowered by a further diffusion of the O adatoms apart from each other. Overcoming a barrier of 0.92 eV and moving to the next bridge site, the total system energy is lowered by 0.72 eV. After the whole relaxing process, the system reaches the ground state configuration with an $E_{ad}(O)$ of −4.49 eV. The relaxed O adatom can migrate along the Mn^{4+}−O^4 channel between two inequivalent bridge sites with barriers of 0.92 and 1.64 eV alternatively. On the basis of these discussions, the $(100)^{4+}$ surface has strong interaction with external O species.
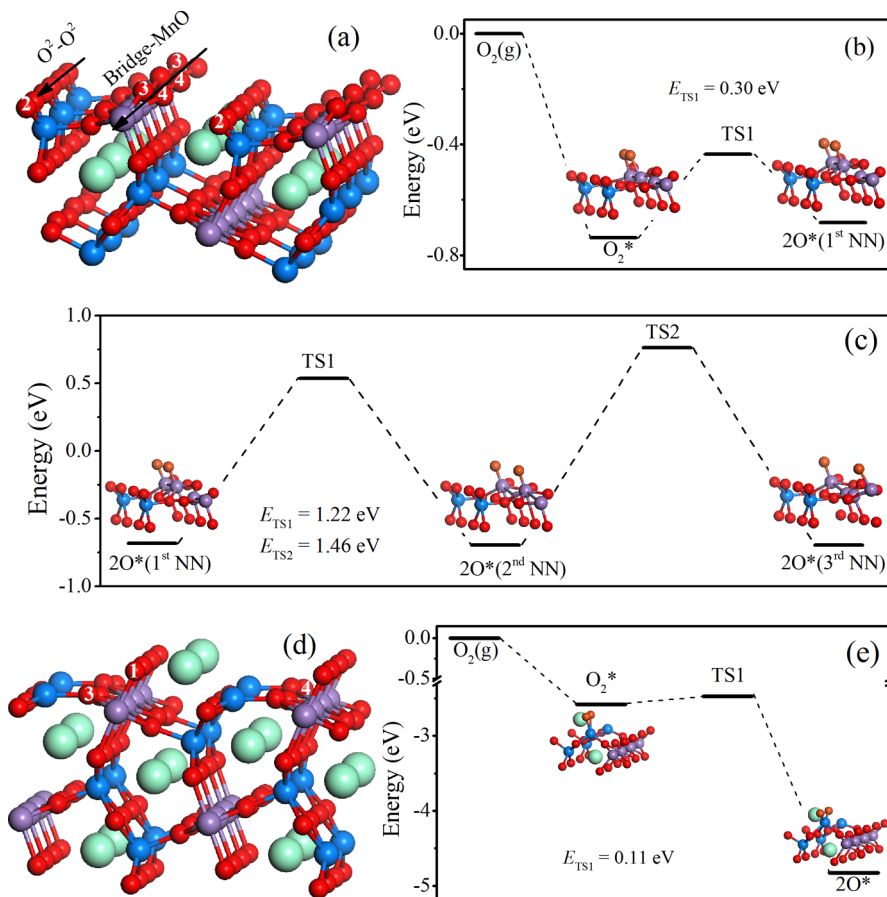
Figure 4. (a) Atomic structure of the $(010)^{4+}$ surface. (b) MEP of adsorption and dissociation of an O_2 molecule on the $(010)^{4+}$ surface. (c) MEP of migration of one adsorbed O atom along the bridge-MnO channel. (d) Atomic structure of the $(010)^{3+}$ surface. (e) MEP of adsorption and dissociation of an O_2 molecule on the $(010)^{3+}$ surface.

Even an unrelaxed O adatom has an $E_{ad}(O)$ stronger than 2.5 eV. Therefore, the Mn ion channel on $(100)^{4+}$ is not expected to be active for oxidation catalysis because of the difficulty of removing adsorbed O atoms. However, The O^2-O^2 channel may supply activities through MvK mechanism considering the relative low $E_{V_O}(O^2)$.

The fact that the lowest $E_{V_O}(O^4)$ is 3.46 eV suggests that the $(100)^{3+}$ surface essentially does not exchange an oxygen species with the external environment. Note that Mn^{3+} ions on the $(100)^{3+}$ surface are directly exposed to the gas phase and are the only possible adsorption sites for O_2 molecules. As shown in Figure 3e, we have calculated the adsorption energy of an O_2 molecule. $E_{ad}(O_2)$ is only −1.01 eV on the $(100)^{3+}$ surface, much lower than that on the $(110)^{3+}$ surfaces. Furthermore, it is not very difficult to dissociate an adsorbed O_2 because E_{dis} is 0.86 eV, and the dissociation on the $(100)^{3+}$ surface is slightly exothermic, with the total energy lowered by 0.31 eV. The O adatom does not bind strongly to the Mn^{3+} ion because the average $E_{ad}(O)$ is −0.66 eV. Similar to the $(110)^{3+}$ surface, there is no diffusion channel for O adatoms on the $(100)^{3+}$ surface because the distance between two neighboring Mn^{3+} ions is as large as 7 Å. According to the above discussions, the $(100)^{3+}$ surface may have activities for NO oxidation through ER mechanism.

As shown in Figure 3e, during the dissociation of an O_2 molecule, the Mn^{3+} ion is gradually pulled out from the surface. The same phenomenon has been observed on all surfaces

studied in the present work, that is, the Mn^{3+} ions experience more severe deformation than Mn^{4+} ions. It may be attributed to the fact that the dissociated O atoms would require more valence electrons than what the Mn ions on the surfaces can supply. These involved Mn ions thus protrude from surfaces and become more isolated from subsurface oxygen so that they can share more electrons with attached O atoms. As a result, stronger Mn−O bonds can form and overcompensate the elastic energy of the deformation. Because Mn^{3+} ions are usually bonded to two external O atoms, they will deform more severely than the Mn^{4+} ions.

(010) Surfaces. Structures of the $(010)^{4+}$ and the $(010)^{3+}$ surfaces are shown in Figure 4a,d, respectively. On the $(010)^{4+}$ surface, there is a bridge-MnO channel containing O^3 and O^4 sites that is similar to that on the $(110)^{4+}$ surface. There is also another O^2-O^2 channel on this surface on top of the Mn^{3+} ions. As listed in Table 1, the V_O at the O^2 site on the $(010)^{4+}$ surface has a low $E_{V_O}(O^2)$ of 1.14 eV, much lower than $E_{V_O}(O^3)$ (2.15 eV) and $E_{V_O}(O^4)$ (2.86 eV). Clearly, V_O's would distribute mainly in the O^2-O^2 channel. Similar to the $(100)^{4+}$ surface, an O atom nearest to the vacancy in the O^2-O^2 channel would move to the atop position of a Mn^{3+} ion (see Figure S2 in the SI). This relocated O atom is also bound much more strongly to the Mn^{3+} ion and requires 2.65 eV to be removed. Because of the long distance between the Mn^{3+} ions, the V_O's in the O^2-O^2 channel can be considered immobile.
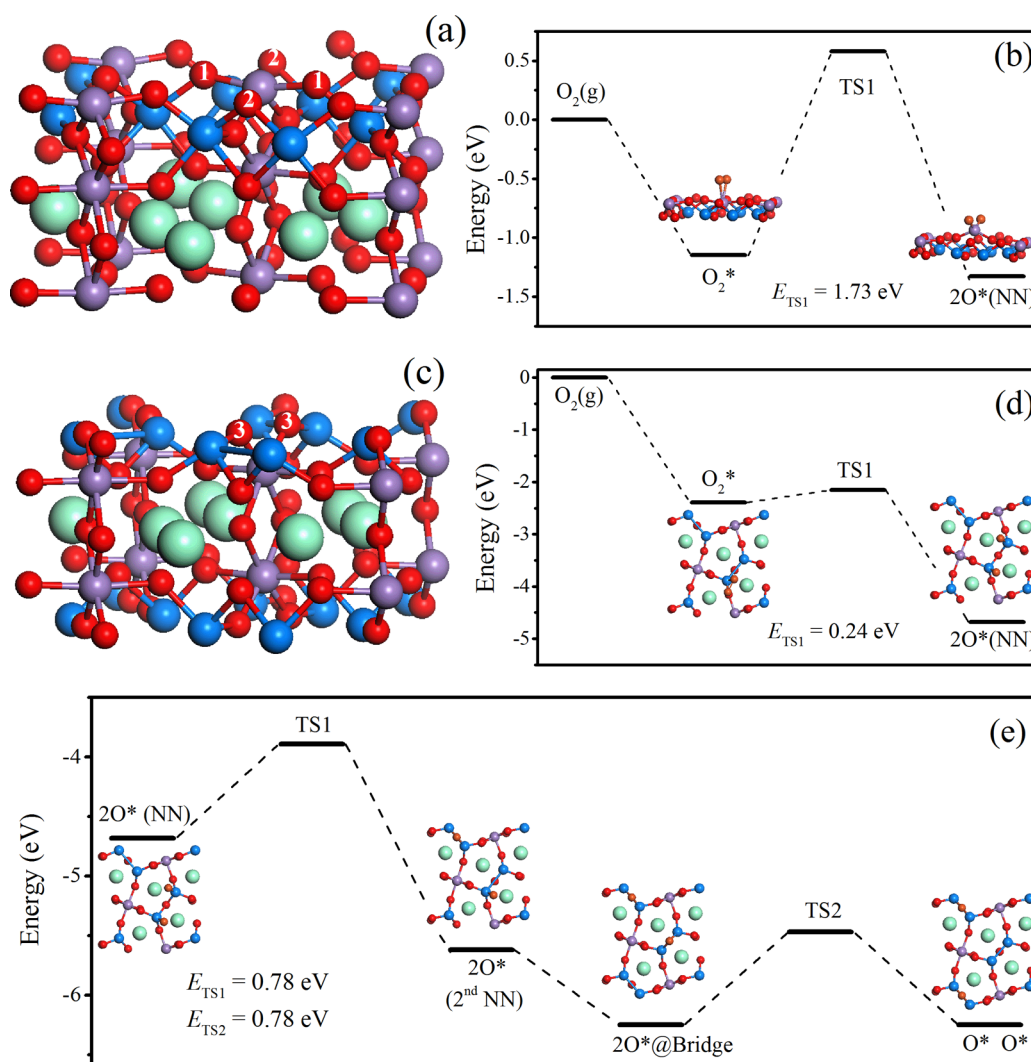
Figure 5. (a) Atomic structure of the $(001)^{4+}$ surface. (b) MEP of adsorption and dissociation of an O_2 molecule on the $(001)^{4+}$ surface. (c) Atomic structure of the $(001)^{3+}$ surface. (d, e) MEP of adsorption and dissociation of an O_2 molecule and MEP of adsorbed O atoms migration on the $(001)^{3+}$ surface, respectively.

On the other hand, although the bridge-MnO channel is difficult for the vacancy creation, it serves as the only possible site for O_2 molecular adsorption on this surface. Figure 4b,c presents the diagram of the evolution of an O_2 molecule on the bridge-MnO channel. The adsorption energy, $E_{ad}(O_2)$, is −0.74 eV. The barrier for dissociation of adsorbed O_2 is 0.30 eV. Both dissociated O atoms are located at atop position of two adjacent Mn^{4+} ions. Interestingly, the dissociation along the bridge-MnO channel is endothermic. On average, the adsorption energy of each O adatom is as low as −0.34 eV. In contrast to the $(110)^{4+}$ surface, O adatoms are not stable at the bridge sites between two Mn^{4+} ions because of the repulsion from lattice O atoms at the O^3 and O^4 sites, as shown in Figure 4a. In addition, these lattice O atoms along the bridge-MnO channel also hinder the migration of an O adatom, as well. Figure 4c shows that when an O adatom migrates along this channel, it needs to overcome 1.22 and 1.46 eV barriers corresponding to hopping over O^3 and O^4 sites, respectively. On the basis of these discussions, the $(010)^{4+}$ surface is expected to have catalytic activities for NO oxidation in different working conditions.

Under O-poor conditions, the O^2−O^2 channel supplies O atoms for the oxidation but will lose the activity in extended cycles because of the reconstruction. Under O-rich conditions, on the other hand, external O_2 molecules may adsorb to the bridge-MnO channel and dissociate to supply O atoms for oxidation as a result of the low dissociation barrier and the weak binding of the O adatoms. One should note that the O^2 sites on the $(010)^{4+}$ surface also have an E_{V_O} that is exceptionally lower than those in bulk. The migration of V_O from the bulk to the $(010)^{4+}$ surface is thus thermodynamically possible. As shown in Figure 4a, the possible diffusion pathways are migration of V_O from O^1 and O^3 vacancies beneath the surface. As shown in Figure 1, the barriers of O^1−O^2 and O^3−O^2 are 1.04 and 2.32 eV, respectively. Although migration from the O^3 sites is unlikely, vacancies from the O^1 sites in the sublayer can migrate to O^2 sites on the $(010)^{4+}$ surface so that there are open sites for O_2 adsorption and dissociation on this surface. Therefore, the V_O diffusion might affect the activities of this surface for NO oxidation. On the other hand, however, the vacancies at O^1 sites in the bulk are expected to be low because of the high E_{V_O} (O^1). It is difficult to estimate the importance of the O^1 (bulk) $\rightarrow$ O^2 (surface) diffusion on the activities of the $(010)^{4+}$
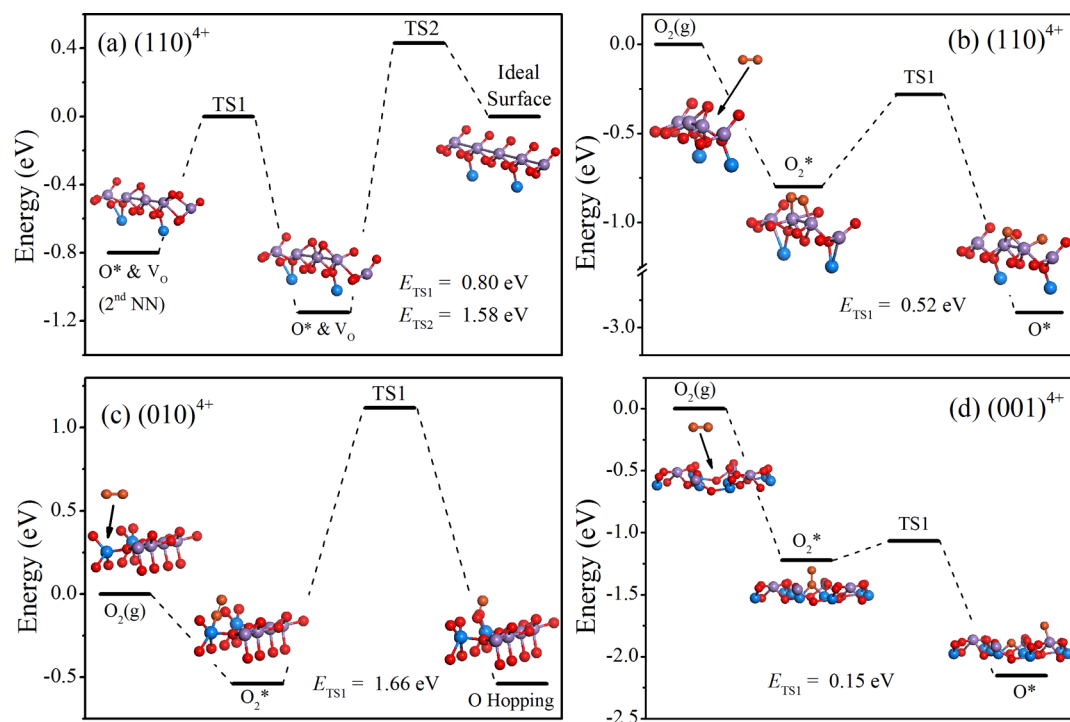
Figure 6. MEPs of external O species on several defective surfaces. (a) One O atom migrates onto the $(110)^{4+}$ surface with a V_O at the O^1 site. (b) One O_2 molecule dissociates on the same surface. (c) One O_2 molecule dissociates on the $(010)^{4+}$ surface with a V_O at the O^2 site. (d) One O_2 molecule dissociates on the $(001)^{4+}$ surface with a V_O at the O^2 site.

surface. A rigorous kinetic model would be needed for a deeper understanding.

For the $(010)^{3+}$ surface, as shown in Figure 4d, O^1 sites are protrusive and form one-dimensional chains. The calculated $E_{V_O}(O^1)$ is 2.17 eV. In addition, although O^3 and O^4 sites are in the sublayer, they are exposed in the vacuum and thus capable of nucleating vacancies. In Table 1, we have also listed $E_{V_O}(O^3)$ and $E_{V_O}(O^4)$, which are 3.28 and 3.75 eV, respectively. The relatively high E_{V_O} indicates that the $(010)^{3+}$ surface is unlikely to contribute its lattice O atoms during the oxidation process. On the other hand, the exposed Mn^{3+} ions are shown to be a strong adsorption site for O_2 molecules because the corresponding adsorption energy $E_{ad}(O_2)$ is −2.64 eV. The adsorbed O_2 molecule can easily dissociate into isolated O atoms with a low barrier of 0.11 eV. Similar to previous discussions, the Mn^{3+} ions are also pulled up from the surface during the O_2 dissociation. The dissociated O atoms are very stable on the Mn^{3+} ion because $E_{ad}(O)$ is −2.46 eV. Therefore, similar to the $(110)^{3+}$ surface, the $(010)^{3+}$ surface can be easily saturated by O species and would not be active for NO oxidation catalysis.

(001) Surfaces. Figure 5a presents the structure of the $(001)^{4+}$ surface. Different from other three orientations, Mn^{4+} ions are isolated on the $(001)^{4+}$ surface. As shown in Table 1, the O^2 site on the $(001)^{4+}$ surface has the lowest E_{V_O} of 0.87 eV compared with all sites considered in the present work. The creation of a vacancy at the O^2 site does not cause a reconstruction. Note that there is no continuous diffusion channel for V_O on the $(001)^{4+}$ surface. The favorable oxygen vacancy formation energy suggests that the $(001)^{4+}$ surface is a good candidate for catalytic activity of oxidation through MvK mechanism. Because $E_{V_O}(O^2)$ is much smaller than all E_{V_O} in

the bulk, we can expect the strong tendency of V_O segregation to the $(001)^{4+}$ surface. As shown in Figure 5a, the O^2 vacancy on the surface may be nucleated from O^2 and O^3 vacancies beneath the surface. However, since the barriers of O^2−O^2 and O^3−O^2 diffusions are 2.2 and 2.3 eV, respectively (shown in Figure 1), the O^2 vacancy nucleation on the $(001)^{4+}$ surface is kinetically not very active. Therefore, V_O diffusion in the bulk may not essentially affect the NO oxidation on $(001)^{4+}$ surface. The exposed Mn^{4+} ions can also serve as adsorption sites for O_2 molecules, with $E_{ad}(O_2) = −1.15$ eV. Surprisingly, the O_2 molecule presents exceptional stability on the $(001)^{4+}$ surface because it requires 1.73 eV to overcome the dissociation barrier, as shown in Figure 5b. The dissociated O atoms do not bond to the Mn^{4+} ion very strongly ($E_{ad}(O) = −0.65$ eV), which may be attributed to the high coverage of the O species on this facet. External O_2 molecules are therefore expected to have minimal activities for NO oxidation because the high dissociation barrier limits the efficiencies.

The structure of the $(001)^{3+}$ surface is presented in Figure 5c. It is the only surface in the present work that contains Mn^{3+} dimers with a Mn−Mn distance of 2.09 Å. Only O^3 sites can be found on this surface, and $E_{V_O}(O^3)$ is calculated to be 3.79 eV. The $(001)^{3+}$ surface thus has a low concentration of V_O's. The exposed Mn^{3+} ions strongly bond to O_2 molecules, with $E_{ad}(O_2) = −2.39$ eV. The adsorbed O_2 molecule, however, can be easily dissociated, and O adatoms can be separated from each other. Figure 5d shows that the dissociation barrier is around 0.24 eV. The dissociated two O adatoms are located at two ends of a Mn^{3+} dimer with an $E_{ad}(O)$ of −2.34 eV. We have also calculated the MEP for further separation, as shown in Figure 5e. One O adatom migrates to the neighboring Mn^{3+} dimer by overcoming a relatively high barrier of 0.78 eV. This further separation allows both O adatoms to relax to the bridge sites of Mn^{3+} dimers. The $E_{ad}(O)$ is enhanced to −3.13 eV. In

addition, two O adatoms are completely isolated from each other because the further separation does not show any difference on the energy scenario compared with the previous configuration. Because of the high E_{V_O} (O^3) and E_{ad}(O), the $(001)^{3+}$ surface does not show catalytic activity for oxidation.

3.3. Replenishment of Oxygen on SmMn$_2$O$_5$ Surfaces.
On the basis of the oxygen chemistry of SmMn$_2$O$_5$ surfaces discussed in previous sections, we can summarize that among different surfaces considered, $(110)^{4+}$, $(010)^{4+}$ $(001)^{4+}$, and $(100)^{3+}$ reveal appropriate vacancy formation energy/oxygen dissociation barrier/binding energy so that they may be active toward NO oxidation. In this section, we devote our attention to the MvK mechanism because it is one of the most common reaction mechanisms in oxides. As listed in Table 1, the first three surfaces have lattice O sites with low vacancy formation energy and are thus capable of supplying O species for oxidation. The $(100)^{3+}$ surface has a high oxygen vacancy formation energy and is excluded from the discussion in this section. Considering a complete NO oxidation catalytic cycle, these surface vacancies must not only be created via the MvK process, but also be replenished by the dissociation of external oxygen species. The creation of vacancies on these sites also causes a local reconstruction, which may lead to a loss of activities. Under working conditions, the behaviors of adsorbed O$_2$ molecules may be different on these defective surfaces from those on ideal ones. To get comprehensive understanding of SmMn$_2$O$_5$ surfaces, it is necessary to study the evolution and replenishment of these defective surfaces in the presence of adsorbed molecular or atomic O.

We first consider the replenishment of oxygen on a $(110)^{4+}$ surface with a single oxygen vacancy. Figure 6a,b presents the MEPs of an O adatom and an O$_2$ molecule migrating on the $(110)^{4+}$ surface with a vacancy in the channel of atop-MnO. The effect of the O$_{Bn}^1$ atom on the migration of the O adatom is local. As shown in Figure 6a, the O adatom migrates along this channel with a barrier of 0.80 eV until it shares one Mn^{4+} ion with the O$_{Bn}^1$ atom, where the adsorption energy of the O adatom increases by 0.35 eV. In addition, a further migration of the O adatom is suppressed because there would be no stable configuration in which the adatom and the O$_{Bn}^1$ atom can share two Mn^{4+} ions. Thus, the vacancy behaves as a trap for an O adatom. In addition, the trapping of an O adatom bifurcates the evolution of the $(110)^{4+}$ surface. The O adatom can either detach from the vacancy by overcoming a barrier of 1.15 eV or destroy the vacancy with a barrier of 1.58 eV to recover to an ideal $(110)^{4+}$ surface. Although these barriers are comparable to each other, the ideal configuration is much less stable. In fact, Figure 6a indicates that the O trapping configuration is the most stable for the $(110)^{4+}$ surface because an ideal one can be transformed to this configuration with a barrier of 0.43 eV. The stronger E_{ad}(O) in the O trapping configuration will degrade the catalytic activities. Therefore, the $(110)^{4+}$ surface cannot sustain reliable activity via the MvK mechanism in extended catalytic cycles.

We have also considered another curing mechanism via combination of an O$_2$ molecule and a single V$_O$ (Figure 6b). After an O$_2$ molecule is adsorbed onto the reconstructed area, it can be dissociated and fill up the vacancy with one dissociated atom. The other O atom slides to the bridge site between the Mn^{4+} ions and becomes a stable adatom. The energy barrier for destroying the vacancy is 0.52 eV. Although filling up O^1 sites by adsorbed oxygen is energetically preferable, the O adatom is

bound to the surface with a binding energy of around 2.8 eV, making it hard to participate in oxidation reactions. It is also hard for the O adatom to destroy another O^1 vacancy because the reaction is a strong endothermal process, as shown in Figure 6a. As a result, the Mn sites along the atop-MnO channel will be gradually occupied by sticky O adatoms in catalytic cycles so that no Mn site would be available for O$_2$ molecules to replenish O^1 vacancies. On the basis of the above discussions, the MvK mechanism on $(110)^{4+}$ is unlikely to prevail.

As discussed in the previous section, there are two channels on the $(010)^{4+}$ surface; however, only O^2 sites have a low enough vacancy formation energy such that the MvK reaction is possible. Figure 6c shows the combination of an O$_2$ molecule and a vacancy at the O^2 site on the $(010)^{4+}$ surface. The O$_2$ molecule adsorbs to one Mn^{3+} ion in a monodentate manner with E_{ad}(O$_2$) of −0.54 eV. The adsorption also suppresses the reconstruction. The total effect of the adsorption is thus to recover the ideal $(010)^{4+}$ surface with one protruding O adatom in the O^2−O^2 channel. The protruding O atom, however, is bound strongly to the channel. The calculated barrier of migration along the channel is as high as 1.66 eV, which makes it hard to migrate to another vacancy site. Therefore, the $(010)^{4+}$ surface is expected to be of only limited catalytic activity for NO oxidation via the MvK mechanism.

Figure 6d presents the evolution process of an O$_2$ molecule adsorbed to the $(001)^{4+}$ surface with a vacancy at the O^2 site. The O$_2$ molecule perpendicularly adsorbs onto the surface with the bottom O atom bonded to two Mn^{3+} ions. The E_{ad}(O$_2$) is −1.22 eV. The other protruding O atom will be further dissociated and migrate to the nearest Mn^{4+} ion. Because the E_{V_O} (O^2) is much lower than the E_{ad}(O), the external O$_2$ molecules tend to fill up the O^2 sites to participate in the oxidation, very similar to the $(110)^{4+}$ surface. The leftover O adatom on an Mn^{4+} ion, however, has a stronger adsorption energy (E_{ad}(O) = −2.15 eV) and, thus, is difficult to remove. It is possible that this adatom can also fill up an O^2 vacancy in later steps. The low barrier for O$_2$ dissociation and the low E_{V_O} suggest that the $(001)^{4+}$ surface is an active surface for catalytic oxidation through MvK mechanism.

3.4. NO Oxidation Mechanism on SmMn$_2$O$_5$ Surfaces.
In the previous sections, we systematically investigated oxygen chemistry on different low-index surfaces of SmMn$_2$O$_5$ to elucidate their catalytic activities toward NO oxidation. To further quantify their contributions to NO oxidation, we first analyzed the thermodynamic stability of these facets because it dictates the area of exposed surface under specific reaction environment (usually represented by chemical potentials (μ) of two components). The total energies and the stoichiometric ratio of the slabs are summarized in Table S1 in the SI. Following the standard procedures pointed out by Noguera et al.,[43] we have constructed the surface stability diagram as functions of $\Delta\mu_O$ and $\Delta\mu_{Mn}$ on the basis of the surface grand potential Ω. The details of construction are presented in the SI. The result is shown in Figure 7. Four surfaces appear in the diagram. At the upper-right corner of the diagram, corresponding to an O-rich and Mn-rich environment, the $(001)^{4+}$ surface is the stable phase, where O and Mn^{4+} atoms coexist in similar amounts. By gradually decreasing the value of $\Delta\mu_{Mn}$ while keeping $\Delta\mu_O$ fixed, the most stable surface becomes the $(010)^{4+}$, where the O species cover almost the whole surface area. The rest of the diagram is filled up by $(100)^{3+}$ and
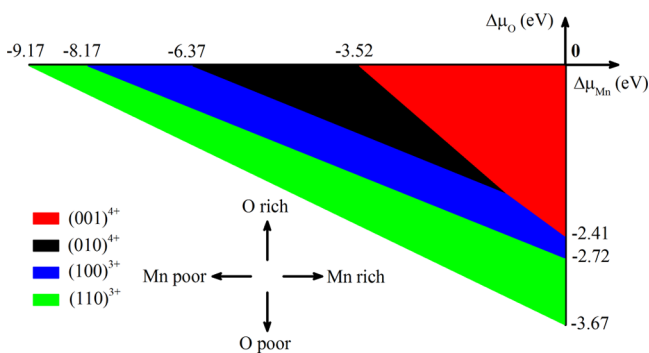
Figure 7. The stability graph of low-index surfaces of SmMn$_2$O$_5$. The actual most stable termination is represented as a function of the excess O and Mn chemical potentials, $\Delta\mu_O$ ($\Delta\mu_O = \mu_O - \mu_O^0$, vertical) and $\Delta\mu_{Mn}$ ($\Delta\mu_{Mn} = \mu_{Mn} - \mu_{Mn}^0$, horizontal).

$(110)^{3+}$. Both surfaces contain Sm atoms because this part corresponds to Sm-rich environment. Among these facets, $(001)^{4+}$, $(010)^{4+}$, and $(100)^{3+}$ are potentially active surfaces, on the analysis in the previous section, and $(110)^{3+}$ is expected to be inactive. We therefore have further studied the reaction routes of NO oxidation on these three active surfaces.

The CI-NEB results of reaction routes on $(001)^{4+}$, $(010)^{4+}$, and $(100)^{3+}$ surfaces are shown in Figure 8. Previous cluster model studies about the oxidation reactions on oxide have shown the surface oxygen is the radical center for surface oxidations.[52−54] Next, we will focus the NO oxidation on the surface lattice oxygen sites or the active oxygen sites formed by the O$_2$ dissociation. Exposed Sm atoms on some surfaces have not been considered as active sites according to the discussions in SI. On the $(001)^{4+}$ surface, a NO molecule is adsorbed at an O^2 site, as shown in Figure 8a. After overcoming a desorption barrier of 0.15 eV, a NO$_2$ molecule escapes from the $(001)^{4+}$ surface and leaves a V$_O$. In the next step, an O$_2$ molecule is perpendicularly bound to the surface and fills up the V$_O$. The protruding O atom is then dissociated and bound to a Mn^{4+} ion to become an adatom. The second NO molecule prefers to be adsorbed at the O adatom over the recovered O^2 site by 0.84 eV. We therefore follow only this branch of the reaction route. The adsorbed NO molecule and the O adatom effectively form a NO$_2$ molecule attached to the Mn^{4+} ion. Finally, the NO$_2$ molecule escapes from the $(001)^{4+}$ surface by overcoming a 1.01 eV desorption barrier. Clearly, the rate-determining step (RDS) along the whole oxidation route is the desorption of the second NO$_2$ molecule. Both MvK and ER mechanisms contribute to the NO → NO$_2$ oxidation. By employing harmonic transition state theory, one can roughly evaluate the rate constant of NO$_2$ production along this pathway. Because the desorption of the second NO$_2$ molecule has the highest barrier, we focus on only the prefactor of this step. By performing the phonon frequency calculation, the prefactor is obtained as 0.76×10^{13} s^{-1}. The rate constant, r, is thus evaluated at 500 K as 5.0×10^2 s^{-1}. One can expect that the $(001)^{4+}$ surface is gradually covered by NO$_2$ molecules after extended catalytic cycles. Special treatments that can expedite NO$_2$ desorption are desirable to improve the activities of the $(001)^{4+}$ surface.

Figure 8b,c presents the NO → NO$_2$ oxidation route on the O^2−O^2 channel and the bridge-MnO channel on the $(010)^{4+}$ surface, respectively. In the O^2−O^2 channel, the first NO molecule is bound to the O atom at the O^2 site. The formed NO$_2$ molecule is strongly bound to the Mn^{3+} ion, and

therefore, it is required to overcome a 1.15 eV desorption barrier to escape from the $(010)^{4+}$ surface. Subsequently, an O$_2$ molecule fills up the remaining V$_O$ and recovers the surface with an O adatom. Another NO molecule is strongly bound to the O adatom. The formed NO$_2$ molecule can be easily released from the surface after overcoming a 0.55 eV barrier. The desorption causes a deformation of the O^2−O^2 channel, which will be relaxed to an ideal structure, and the total energy is decreased by 1.2 eV. Similar to the $(001)^{4+}$ surface, the dominant oxidation mechanisms in the O^2−O^2 channel are also both MvK and ER. The RDS is the desorption of the first produced NO$_2$ molecule. The prefactors of the NO$_2$ desorption reactions are calculated as 0.64×10^{13} and 0.81×10^{13} s^{-1}, respectively. At 500 K, the rate constants, r, for the first and the second NO$_2$ molecule desorptions are 17 s^{-1} and 2.3×10^7 s^{-1}. Furthermore, because the desorption of the second NO$_2$ molecule is much easier, one should expect that the catalytic activities of O^2−O^2 channel can be raised dramatically if there are large amounts of V$_O$'s at O^2 sites, which is not difficult to satisfy because the E_{V_O} (O^2) on the $(010)^{4+}$ surface is only 1.14 eV.

In the bridge-MnO channel on the $(010)^{4+}$ surface, an O$_2$ molecule is first adsorbed at two Mn^{4+} ions in a bidentate manner then dissociated into two O adatoms on the two adjacent Mn^{4+} ions with a barrier of 0.30 eV. Subsequently, two NO molecules are consecutively bonded to each O adatom, and the resulting NO$_2$ molecules are detached from the surface after overcoming a 0.38 eV barrier. Clearly, the ER mechanism dominates the NO oxidation in the bridge-MnO channel. The RDS has a much lower barrier compared with other potential active sites. Therefore, the bridge-MnO channel on the $(010)^{4+}$ surface has the highest activities for NO oxidation. Maximizing the surface area of the $(010)^{4+}$ would be beneficial to the NO oxidation performance of SmMn$_2$O$_5$. The reaction path in the bridge-MnO channel is special bedcause of the close heights of all three barriers. Therefore, in the evaluation of the rate constant, one needs to consider all the prefactors of these three steps. The prefactors of the three initial states in Figure 8c are 2.8×10^{13} s^{-1} (O$_2$ dissociation), 1.0×10^{13} s^{-1} (first NO$_2$ molecule desorption), and 0.6×10^{13} s^{-1} (second NO$_2$ molecule desorption), respectively. At 500 K, the reaction rates of these three steps are evaluated as 2.65×10^{10}, 1.48×10^9, and 8.87×10^8 s^{-1}, respectively. The overall rate constant is determined by the second NO$_2$ desorption, which is 8.87×10^8 s^{-1}.

Figure 8d shows the energetic scenario of NO → NO$_2$ oxidation on the $(100)^{3+}$ surface. At the beginning, an O$_2$ molecule is adsorbed to a Mn^{3+} ion and then dissociated with a 0.86 eV barrier. Then a NO molecule is attached to one of the O adatoms, and the Mn^{3+}-O bond is stretched from 1.67 to 4.27 Å. In the next step, the formed NO$_2$ molecule is detached from the $(100)^{3+}$ surface with a desorption barrier of 1.17 eV and leaves an O adatom. Another NO molecule is then bonded to the O adatom without substantially stretching the Mn^{3+}−O bond. Finally, the second NO$_2$ molecule escapes from the surface with a little higher barrier of 1.35 eV. The corresponding prefactor is calculated as 4.22×10^{13} s^{-1}. At 500 K, the rate constant of the NO$_2$ desorption is 1.04 s^{-1}. The $(100)^{3+}$ surface then recovers to an ideal structure. The ER mechanism dominates the oxidation route, and the RDS on the $(100)^{3+}$ surface is also the desorption of two NO$_2$ molecules. By comparing rate constants along the oxidation routes, the
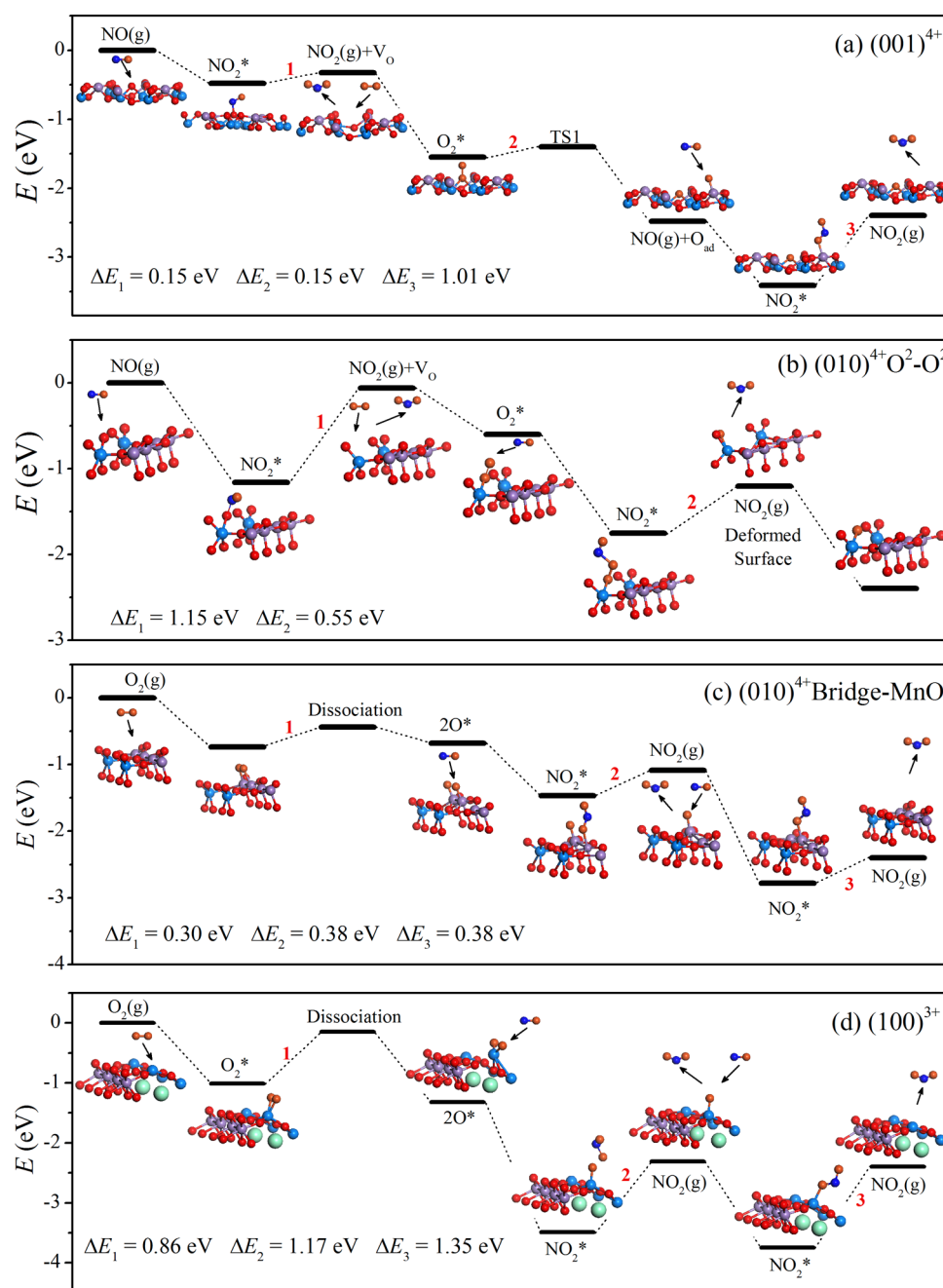
Figure 8. Energetic routes of NO oxidation on (a) $(001)^{4+}$, (b, c) $(010)^{4+}$ and (d) $(100)^{3+}$ surfaces. The total oxidation reactions on all surfaces can be summarized as $2NO + O_2 \rightarrow 2NO_2$, exothermally.

$(100)^{3+}$ surface is expected to have a lower, but still appreciable, contribution to the catalytic activities of $SmMn_2O_5$ for NO oxidation.

According to the above discussions, the rate-determining step along each of the four NO oxidation pathways is the NO_2 desorption. The Mn^{4+} dimer on the $(010)^{4+}$ surface supplies the most active sites for NO oxidation. These observations are similar to the study on $SmMn_2O_5$ of Wang et al.[18] In addition, the barrier of NO_2 desorption is calculated around 1.01 eV ~ 1.35 eV except that along the bridge MnO channel on the $(010)^{4+}$ surface, which is also comparable to the 0.90 eV reported in ref 18. However, one should note that the reduced (110) surface in ref 18. is less stable than those shown in Figure 7 and, thus, is not considered in the current study.

Discussions on Figure 8 also suggest that the consumption of O species from surfaces is essential during the catalysis. Therefore, it is necessary to consider the stability of surfaces with the presence of the reducing agent (NO) in the atmosphere because this relates to the durability of $SmMn_2O_5$ as the catalyst for NO $\rightarrow$ NO_2. To this end, we have employed "constrained thermodynamic equilibrium" to briefly discuss the stability of the three surfaces having relatively a low E_{V_O}—$(100)^{4+}$, $(010)^{4+}$, and $(001)^{4+}$—as a function of the pressure of NO (p_{NO}) and O_2 (p_{O_2}).[55,56] Two temperatures, 300 and 600 K were chosen. The details of the construction process are presented in the SI. The corresponding phase diagrams are displayed in Figure S4. It shows that a very low p_{O_2}

is detrimental to all three surfaces. The $(001)^{4+}$ surface will be affected most severely at 600 K: if the p_{O_2} is lower than 5×10^{-5} atm, the O atoms on the O^2 sites are energetically favorable to sublime to the atmosphere because of the low E_{V_O}. Because a typical p_{O_2} is higher than 10^{-4} atm,[55−57] the sublimation of the O species from the $SmMn_2O_5$ surfaces might not be a severe limitation. On the other hand, the effects of NO are less important. In the case of $p_{O_2} \sim 10^{-2}$ atm and $T = 600$ K, both the $(100)^{4+}$ and $(010)^{4+}$ surfaces can keep their atomic structures in the whole considered range of p_{NO}, meaning that reducing agent NO will not be able to consume all the O species in the surface layer, even if the p_{NO} is around 10^{10} atm. The $(001)^{4+}$ surface under the same conditions ($p_{O_2} \sim 10^{-2}$ atm, $T = 600$ K) can also retain stability, except that p_{NO} is higher than 5×10^8 atm, as shown in Figure S4. On the basis of the above discussions, $SmMn_2O_5$ surfaces with possible MvK activities have reliable stability over a typical range of temperatures and partial pressures of NO.

3.5. Discussions on Activities of $SmMn_2O_5$ Surfaces. In the previous sections, the oxygen vacancy formation energy, E_{V_O}, has been used as an important descriptor for NO oxidation on $SmMn_2O_5$ surfaces. It is necessary to explore the indicator representing the value of E_{V_O} from electronic structure analysis. We have found that the E_{V_O} in the bulk is related to their Bader charge. Therefore, we have calculated the Bader charge $Q(e)$ of surface oxygen atoms and list the results in Table 1. We have also plotted the Q and the corresponding oxygen formation energy in Figure 9. The overall trend is that oxygen sites with a
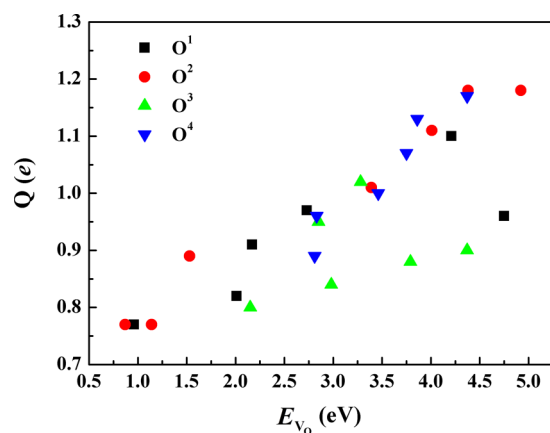

Figure 9. The relationship between Bader charge and E_{V_O} on different sites on different surfaces of $SmMn_2O_5$.

higher $Q(e)$ have a higher E_{Ov}: as shown in Figure 9, E_{V_O} is approximately proportional to Q. For example, $E_{V_O}(O^2)$ on the $(001)^{4+}$ surface, $E_{V_O}(O^1)$ on the $(110)^{4+}$ surface, and $E_{V_O}(O^2)$ on the $(010)^{4+}$ surface have the three lowest formation energies, and share the lowest Q on the corresponding O sites before the nucleation of the oxygen vacancies. Furthermore, most O sites with E_{V_O} higher than 4.3 eV have a Bader charge higher than $1.1e$, whereas those with an E_{V_O} between 3 and 4 eV have a Bader charge of $\sim 1.0e$. Overall, the Bader charge of O atoms on surfaces is a reasonable indicator to represent the activities of a surface by the MvK mechanism.

4. CONCLUSION

In summary, we have studied the stability and mobility of the O species in the bulk phase and four low-index surface families of $SmMn_2O_5$. The detailed oxygen chemistry, including its molecular adsorption, dissociation, and replenishment of formed vacancies are discussed in detail. The $(001)^{4+}$, $(010)^{4+}$, and $(100)^{3+}$ surfaces have the lowest barriers against exchanging O species with environments and, thus, are expected to be active surfaces. On the basis of the above discussions, we have further calculated the reaction routes along different channels on these three surfaces. The results show that the bridge-MnO channel on the $(010)^{4+}$ surface has the lowest barrier via the ER mechanism. The $(001)^{4+}$ surface and the $O^2–O^2$ channel on the $(010)^{4+}$ surface also considerably contribute to the total oxidation rate through synergetic ER and MvK mechanisms. We have also identified that on all active sites, the rate-limiting step in the NO → NO_2 reaction is the NO_2 desorption due to relatively strong Mn−O interactions. Moreover, we have found that the Bader charge of O atoms on surfaces can be regarded as an indicator to evaluate the activities of the surface by the MvK mechanism. In addition, the current study does not indicate the sensitivity of the catalytic activities on the valence status of Mn ions. Our study presents systematic pictures on catalytic activities of $SmMn_2O_5$, which are important to the full understanding and improvement of $SmMn_2O_5$ performance. A comprehensive microkinetic model on the reaction dynamics of $SmMn_2O_5$ is under construction and will be discussed in future publications.

■ ASSOCIATED CONTENT

ⓢ Supporting Information

The Supporting Information is available free of charge on the ACS Publications website at DOI: 10.1021/acscatal.5b00249.

Details of building up surface grand potential diagram, atomic structures of defective surfaces, and atomic coordinates of slabs we used in our calculations (PDF)

■ AUTHOR INFORMATION

Corresponding Authors
*E-mail: rongchen@mail.hust.edu.cn.
*E-mail: bshan@mail.hust.edu.cn.

Author Contributions
⊥Z.C. and X.L. contributed equally to this work.

Notes
The authors declare no competing financial interest.

■ ACKNOWLEDGMENTS

■ REFERENCES

(1) Fernández-García, M.; Martínez-Arias, A.; Hanson, J. C.; Rodriguez, J. A. *Chem. Rev.* **2004**, *104*, 4063−4104.

(2) Wang, H. F.; Kavanagh, R.; Guo, Y. L.; Guo, Y.; Lu, G. Z.; Hu, P. *J. Catal.* **2012**, *296*, 110−119.

(3) Zhu, J.; Li, H.; Zhong, L.; Xiao, P.; Xu, X.; Yang, X.; Zhao, Z.; Li, J. *ACS Catal.* **2014**, *4*, 2917−2940.

(4) Malavasi, L.; Fisher, C. J.; Saiful Islam, M. *Chem. Soc. Rev.* **2010**, *39*, 4370−4387.

(5) Xie, X.; Li, Y.; Liu, Z. Q.; Haruta, M.; Shen, W. *Nature* **2009**, *458*, 746−749.

(6) Jansson, J.; Palmqvist, A. E. C.; Fridell, E.; Skoglundh, M.; Österlund, L.; Thormählen, P.; Langer, V. *J. Catal.* **2002**, *211*, 387−397.

(7) Goodman, D. W.; Peden, C. H. F. *J. Phys. Chem.* **1986**, *90*, 4839−4843.

(8) Reuter, K.; Scheffler, M. *Phys. Rev. B: Condens. Matter Mater. Phys.* **2006**, *73*, 045433.

(9) Misono, M.; Hirao, Y.; Yokoyama, C. *Catal. Today* **1997**, *38*, 157−162.

(10) Qi, G. S.; Yang, R. T. *J. Catal.* **2003**, *217*, 434−441.

(11) Lahousse, C.; Bernier, A.; Grange, P.; Delmon, B.; Papaefthimiou, P.; Ioannides, T.; Verykios, X. *J. Catal.* **1998**, *178*, 214−225.

(12) Kim, C. H.; Qi, G. S.; Dahlberg, K.; Li, W. *Science* **2010**, *327*, 1624−1627.

(13) Adler, S. B. *Chem. Rev.* **2004**, *104*, 4791−4844.

(14) Han, J. W.; Yildiz, B. *Energy Environ. Sci.* **2012**, *5*, 8598−8607.

(15) Zhou, J.; Chen, G.; Wu, K.; Cheng, Y. *J. Phys. Chem. C* **2013**, *117*, 12991−12999.

(16) Choi, Y. M.; Lin, M. C.; Liu, M. L. *J. Power Sources* **2010**, *195*, 1441−1445.

(17) Lee, Y. L.; Kleis, J.; Rossmeisl, J.; Morgan, D. *Phys. Rev. B: Condens. Matter Mater. Phys.* **2009**, *80*, 224101.

(18) Wang, W. C.; McCool, G.; Kapur, N.; Yuan, G.; Shan, B.; Nguyen, M.; Graham, U. M.; Davis, B. H.; Jacobs, G.; Cho, K.; Hao, X. H. *Science* **2012**, *337*, 832−835.

(19) Masel, R. I. Introduction of Surface Reaction. In *Principles of Adsorption and Reaction on Solid Surfaces*; Wiley-Interscience: New York, 1996; pp 438−477.

(20) Ding, W. C.; Gu, X. K.; Su, H. Y.; Li, W. X. *J. Phys. Chem. C* **2014**, *118*, 12216−12223.

(21) Shan, B.; Zhao, Y.; Hyun, J.; Kapur, N.; Nicholas, J.; Cho, K. *J. Phys. Chem. C* **2009**, *113*, 6088−6092.

(22) Mars, P.; Van Krevelen, D. W. *Chem. Eng. Sci.* **1954**, *3*, 41−59.

(23) Zhao, M.; Shen, M.; Wang, J. *J. Catal.* **2007**, *248*, 258−267.

(24) Chen, F.; Liu, D.; Zhang, J.; Hu, P.; Gong, X. Q.; Lu, G. Z. *Phys. Chem. Chem. Phys.* **2012**, *14*, 16573−16580.

(25) Choi, S. O.; Penninger, M.; Kim, C. H.; Schneider, W. F.; Thompson, L. T. *ACS Catal.* **2013**, *3*, 2719−2728.

(26) Chen, Z. Z.; Kim, C. H.; Thompson, L. T.; Schneider, W. F. *Surf. Sci.* **2014**, *619*, 71−76.

(27) Liu, X.; Chen, Z. Z.; Wen, Y. W.; Chen, R.; Shan, B. *Catal. Sci. Technol.* **2014**, *4*, 3687−3696.

(28) Zhou, C.; Liu, X.; Wu, C. Z.; Wen, Y. W.; Xue, Y.; Chen, R.; Zhang, Z. L.; Shan, B.; Yin, H. F.; Wang, W. G. *Phys. Chem. Chem. Phys.* **2014**, *16*, 5106−5112.

(29) Pilania, G.; Gao, P. X.; Ramprasad, R. *J. Phys. Chem. C* **2012**, *116*, 26349−26357.

(30) Pai, W. W.; Bartelt, N. C.; Peng, M. R.; Reutt-Robey, J. E. *Surf. Sci.* **1995**, *330*, L679−L685.

(31) Hohenberg, P.; Kohn, W. *Phys. Rev.* **1964**, *136*, B864−B871.

(32) Kohn, W.; Sham, L. J. *Phys. Rev.* **1965**, *140*, A1133−A1138.

(33) Kresse, G.; Hafner, J. *Phys. Rev. B: Condens. Matter Mater. Phys.* **1993**, *47*, 558−561.

(34) Kresse, G.; Hafner, J. *Phys. Rev. B: Condens. Matter Mater. Phys.* **1994**, *49*, 14251−14269.

(35) Kresse, G.; Furthmüller, J. *Comput. Mater. Sci.* **1996**, *6*, 15−50.

(36) Perdew, J. P.; Burke, K.; Ernzerhof, M. *Phys. Rev. Lett.* **1996**, *77*, 3865−3868.

(37) Kresse, G.; Joubert, D. *Phys. Rev. B: Condens. Matter Mater. Phys.* **1999**, *59*, 1758−1775.

(38) Monkhorst, H. J.; Pack, J. D. *Phys. Rev. B* **1976**, *13*, 5188−5192.

(39) Aryasetiawan, F.; Gunnarsson, O. *Rep. Prog. Phys.* **1998**, *61*, 237.

(40) Onida, G.; Reining, L.; Rubio, A. *Rev. Mod. Phys.* **2002**, *74*, 601.

(41) Heyd, J.; Scuseria, G. E.; Ernzerhof, M. *J. Chem. Phys.* **2003**, *118*, 8207−8215.

(42) Heyd, J.; Scuseria, G. E.; Ernzerhof, M. *J. Chem. Phys.* **2006**, *124*, 219906.

(43) Bottin, F.; Finocchi, F.; Noguera, C. *Phys. Rev. B: Condens. Matter Mater. Phys.* **2003**, *68*, 035418.

(44) Chen, G. H.; Hou, Z. F.; Gong, X. G. *Comput. Mater. Sci.* **2008**, *44*, 46−52.

(45) Henkelman, G.; Jónsson, H. *J. Chem. Phys.* **2000**, *113*, 9978−9985.

(46) Kagomiya, I.; Kohn, K.; Uchiyama, T. *Ferroelectrics* **2002**, *280*, 131−143.

(47) Alonso, J. A.; Casais, M. T.; Martínez-Lope, M. J.; Martínez, J. L.; Fernández-Díaz, M. T. *J. Phys.: Condens. Matter* **1997**, *9*, 8515−8526.

(48) Jia, L. C.; Wang, X.; Li, W. L.; Li, K.; Chi, B.; Pu, J.; Jian, L.; Yuan, S. L. *J. Power Sources* **2014**, *253*, 138−142.

(49) Henkelman, G.; Arnaldsson, A.; Jonsson, H. *Comput. Mater. Sci.* **2006**, *36*, 354−360.

(50) Zhu, G. Q.; Liu, P.; Hojamberdiev, M.; Ge, B.; Liu, Y.; Miao, H. Y.; Tan, G. Q. *Mater. Chem. Phys.* **2009**, *118*, 467−472.

(51) Hensley, A. J. R.; Hong, Y. C.; Zhang, R. Q.; Zhang, H.; Sun, J. M.; Wang, Y.; McEwen, J. S. *ACS Catal.* **2014**, *4*, 3381−3392.

(52) Hirabayashi, S.; Ichihashi, M. *J. Phys. Chem. A* **2013**, *117*, 9005−9010.

(53) Dong, F.; Heinbuch, S.; Xie, Y.; Rocca, J. J.; Bernstein, E. R.; Wang, Z. C.; Deng, K.; He, S. G. *J. Am. Chem. Soc.* **2008**, *130*, 1932−1943.

(54) Xie, Y.; Dong, F.; Heinbuch, S.; Rocca, J. J.; Bernstein, E. R. *Phys. Chem. Chem. Phys.* **2010**, *12*, 947−959.

(55) Reuter, K.; Scheffler, M. *Appl. Phys. A: Mater. Sci. Process.* **2004**, *78*, 793−798.

(56) Piccinin, S.; Zafeiratos, S.; Stampfl, C.; Hansen, T.; Hävecker, M.; Teschner, R.; Bukhtiyarov, V.; Girgsdies, F.; Knop-Gericke, A.; Schlögl, R.; Scheffler, M. *Phys. Rev. Lett.* **2010**, *12*, 947−959.

(57) Hendriksen, B. L. M. *Model Catalysts in Action: High-Pressure Scanning Tunneling Microscopy*, Ph.D. thesis, Universiteit Leiden, 2003; pp 133−135.